# A Stabilizing α/β-Hydrophobic Core Greatly Contributes to Hyperthermostability of Archaeal [P62A]Ssh10b[†,‡]

Xianyang Fang,[§,∥] Qiu Cui,[§,∥] Yufeng Tong,[∥] Yingang Feng,[∥] Lu Shan,[∥] Li Huang,[⊥] and Jinfeng Wang*[,∥]

*National Laboratory of Biomacromolecules, Institute of Biophysics, Chinese Academy of Sciences, 15 Datun Road, Beijing 100101, China, and State Key Laboratory of Microbial Resources, Institute of Microbiology, Chinese Academy of Sciences, Beijing 100080, China*

*Received April 29, 2008; Revised Manuscript Received September 5, 2008*

ABSTRACT: The hyperthermophilic Ssh10b from *Sulfolobus shibatae* is a member of the Sac10b family, which has been postulated to play a role in chromosomal organization in Archaea. Ssh10b is capable of significantly constraining negative DNA supercoils at elevated temperatures. In this study, the solution structure of the dimeric P62A mutant Ssh10b ([P62A]Ssh10b) was determined by multidimensional NMR spectroscopy. The backbone $^{15}N$ dynamics, H/D exchange with and without the denaturant GdmSCN, and chemical and thermal denaturation experiments were performed to investigate the molecular basis of high thermostability of [P62A]Ssh10b. Data analysis has revealed an α/β-hydrophobic core consisting of two α-helices and one β-sheet which are stabilized by cooperative hydrophobic and hydrogen-bonding interactions. This stabilizing α/β-hydrophobic core of [P62A]Ssh10b exhibiting highly restricted internal motions is composed of residues having highly protected amide protons which exchange with solvent mostly by means of a global unfolding process. The K40N mutation greatly destabilizes the mutant [P62A]Ssh10b because this mutation disturbs the packing of α-helix against the β-sheet reducing the stability of the α/β-hydrophobic core in the mutant protein. In comparison with homologous mesophilic and thermophilic proteins, it can be presumed that the stabilizing α/β-hydrophobic core in the [P62A]Ssh10b structure greatly contributes to the high thermostability of the protein.

Proteins having molecular mass of 7, 8, and 10 kDa have been extracted from the thermoacidophilic archaebacterium *Sulfolobus acidocaldarius* grown at 75−80 °C and pH 4.5−4.8. Sac10b is the second most abundant protein in *S. acidocaldarius* (*1*). The members of Sac10b family, postulated as chromosomal DNA binding proteins, are highly conserved among most archaeal and eukaryal proteins having homologous sequences identified from higher plants, protists, and vertebrates (*2, 3*). Ssh10b and Sso10b are the members of the Sac10b family. Ssh10b has been isolated from *Sulfolobus shibatae* and Sso10b having identical sequence to Ssh10b with the exception of amino acids 1−3 has been isolated from *Sulfolobus solfataricus* (*2, 4*). Sso10b was found to exist predominantly in an acetylated form in vivo and in deacetylated form after incubation with Sir2 in the presence of $NAD^+$, regulating the DNA binding affinity (*2, 5, 6*). More recently, the crystal structures of Sso10b (also named Alba) have been published (*7*), which show structural homology with the C-terminal domain of the *Escherichia coli* translation factor IF3 and the N-terminal DNA-binding domain of DNase I. Ssh10b, a protein thermally stable up to 402 K (*8*), binds DNA without apparent sequence specificity, and is capable of significantly constraining negative DNA supercoils at elevated temperatures (*4*). The previous NMR studies (*9, 10*) have revealed that two forms of Ssh10b homodimer coexisted in solution, and the slow cis−trans isomerization of the L61−P62 peptide bond is responsible for the conformational heterogeneity of the Ssh10b homodimer. The P62A mutant Ssh10b ([P62A]-Ssh10b) adopted only the trans-form homodimer. Similar to Ssh10b, [P62A]Ssh10b is a highly thermostable protein and shows the same features upon interaction with DNA at high temperatures (*10*). However, what leads to the high thermostability of these proteins has not been deciphered clearly.

The present study is aimed at understanding the molecular origin of the extreme thermostability of [P62A]Ssh10b in structure term. For this purpose, the solution structure of [P62A]Ssh10b was determined by multidimensional NMR spectroscopy. The NMR experiments including amide hydrogen exchange with and without the denaturant GdmSCN and backbone $^{15}N$ relaxation as well as chemical and thermal denaturation experiments were adopted in this study. On the basis of the solution structure of [P62A]Ssh10b dimer and homologue sequences comparison, the molecular basis of the high thermostability of [P62A]Ssh10b is discussed.

[†] This research was supported by the National Natural Science Foundation of China (NNSFC 30270301), and partially by the Key Important Project from Chinese Academy of Sciences (Grant KSCX1-SW-17).

[‡] The atomic coordinates of [P62A]Ssh10b have been deposited in the Protein Databank (accession code 1Y9X).

* To whom correspondence should be addressed. E-mail: jfw@sun5.ibp.ac.cn. Phone: 86-10-64888490. Fax: 86-10-64872026.

[§] These authors contributed equally to this work.

[∥] Institute of Biophysics, Chinese Academy of Sciences.

[⊥] Institute of Microbiology, Chinese Academy of Sciences.

10.1021/bi8007593 CCC: $40.75 
Published on Web 09/27/2008

## MATERIALS AND METHODS

*Sample Preparation.* The expression and purification of $^{15}N$ and $^{13}C$ single and double labeled [P62A]Ssh10b have been reported previously (*10*). The K40N mutant [P62A]-Ssh10b ([K40N/P62A]Ssh10b) was obtained using the same protocol. The purity of the proteins was checked by SDS-PAGE to be a single band and by agarose gel electrophoresis to be free of nucleic acid contaminants.

Samples used for NMR experiments were as follows: 1 mM $^{15}N$-labeled [P62A]Ssh10b in 90% $H_2O$/10% $D_2O$ containing 20 mM acetate buffer, 20 mM KCl, and 50 $\mu$M $NaN_3$; 1 mM $^{13}C$-labeled [P62A]Ssh10b in 99.996% $D_2O$ containing 20 mM acetate buffer, 20 mM KCl, and 50 $\mu$M $NaN_3$; 1 mM $^{15}N$ and $^{13}C$ double labeled [P62A]Ssh10b in 90% $H_2O$/10% $D_2O$ containing 20 mM acetate buffer, 20 mM KCl, and 50 $\mu$M $NaN_3$. The pH of all NMR samples was about 4.8.

For hydrogen exchange measurement in $D_2O$, the freshly prepared 1 mM $^{15}N$-labeled [P62A]Ssh10b was lyophilized to dryness and redissolved in 100% $D_2O$ immediately prior to NMR experiments at 310 K. For hydrogen exchange measurement in the presence of GdmSCN, the deuterated GdmSCN was prepared by lyophilizing three times of GdmSCN predissolved in 100% $D_2O$. The refractive index measurement was used to determine the concentration of deuterated GdmSCN (*11*). The freshly prepared $^{15}N$-labeled [P62A]Ssh10b was dissolved in 100% $D_2O$ solution containing deuterated GdmSCN of various concentrations.

*NMR Spectroscopy.* All NMR experiments were performed at 310 K on a Bruker DMX 600 NMR spectrometer equipped with a triple resonance cryo-probe. The 3D $^1H-^{15}N-^{13}C$ HNCO, HNCA, HN(CA)CO, HNCACB, CBCA(CO)NH, C(CO)NH, HBHANH, and HBHA(CO)NH spectra, and 3D $^1H-^{13}C$ HCCH-TOCSY and HCCH-COSY spectra (*12*) were recorded for backbone and side chain resonance assignments. The 3D $^1H-^{15}N$ HNHA experiment (*13*) was carried out for measurements of the $^3J_{HN\alpha}$ coupling constant. The 3D $^1H-^{15}N$ NOESY-HSQC and $^1H-^{13}C$ NOESY-HMQC experiments ($\tau_m = 80$ ms) were used for obtaining the NOE distance restraints. A modified four-dimensional experiment $^1H,^{13}C$-HMQC-$^1H,^1H$-NOESY-$^1H,^{15}N$-HSQC experiment was performed with the $^{15}N/^{13}C$-asymmetrically labeled protein for determining residues involved in the dimer interface. The slowly H/D exchange experiments were performed for estimation of hydrogen bond restraints.

The measurements of $^{15}N$ $T_1$ and $T_2$ and $^1H-^{15}N$ NOE relaxation parameters were performed for [P62A]Ssh10b and [K40N/P62A]Ssh10b at 310 K using the standard methods (*14*). For $^{15}N$ $T_1$ measurements, the delay times were set to 24, 124, 142, 282, 382, 522, 822, 1202, and 1602 ms, whereas for $T_2$ measurements, the relaxation delays were 17, 34, 25.4, 33.9, 50.9, 67.8, 84.8, 101.8, 118.7, 135.7, and 152.6 ms. In the 2D $^1H-^{15}N$ NOE experiments, a delay of 4 s was followed by $^1H$ saturation for 6 s, whereas the saturation period was replaced by a delay of equivalent duration in the control experiment. Two experiments were run in an interleaved manner. For amide proton H/D exchange measurements, a series of 2D $^1H-^{15}N$ HSQC spectra for [P62A]Ssh10b in the absence and presence of deuterated GdmSCN were recorded at 310 K. The H/D exchange measurements for samples without GdmSCN were carried out over a 14 days period which was divided into subseries with time regions of 2.5 days and 2.5−14 days. The spectra recorded over a 2.5 day period were successively obtained after every 12 min, those over 2.5−14 day period were obtained at different time intervals from starting times of the measurement. Each 2D spectrum required 1000 s to complete. The $^1H-^{15}N$ resonance signals for samples with deuterated GdmSCN were detected as a function of time as they decayed to values beyond detection.

The NMR data were processed and analyzed with FELIX 98 software (Accelrys Inc.). $^1H$ chemical shifts were referenced to internal DSS. $^{15}N$ and $^{13}C$ chemical shifts were obtained indirectly (*15*).

*Structure Calculations.* The NOEs used in the structure calculation were identified in a manner combining manual and semiautomatic assignments using in-house macros together with ARIA1.2 (*15*−*17*). Initially, 1151 unambiguous NOEs were assigned, and remaining unassigned NOEs were treated as ADRs (ambiguous distance restraints). These NOE restraints with 53 dihedral and 26 hydrogen bond restraints were used as input for ARIA iterative calculation of monomer structures (*16*−*18*). In each of the 8 iterations, 50 structures were calculated, 10 structures with low energies were kept and used as the template structures for next iteration, and the 7 best structures were used for violation analysis. For docking the two monomer structures into a dimer structure, the determined intermolecular NOEs were applied and the intermolecular NOE assignments made by ARIA calculation were used for iterative calculation while keeping the dihedral and hydrogen bond restraints. The potential intermolecular NOEs across the dimer interface as ambiguous distance restraints were applied to the symmetry ADR protocols in ARIA calculation (*19*). Over 2228 unambiguous and 533 ambiguous including 55 intermolecular nonredundant NOE distance restraints were obtained and used for final structure calculations. The stereospecific assignments for prochiral groups were made using a floating chirality approach (*20*). A family of 150 structures was calculated using a simulated annealing protocol and 20 structures with low energies were selected for further refinement using the force field for electrostatic and van der Waal's interactions (*21*). Quality of the 20 NMR-derived structures was evaluated using the program PROCHECK (*22*).

*Analysis of $^{15}N$ Relaxation Data.* The relaxation rate constants $R_1$ and $R_2$ and $^1H-^{15}N$ NOE values were determined according the procedures as described (*23*). An initial estimate of the magnitude and orientation of the rotational diffusion tensor was obtained from the $R_2/R_1$ ratios using the program TENSOR2.0 (*24*) following the fitting protocol described by Pawley et al. (*25*). The resulting diffusion parameters and the $R_1$, $R_2$, and NOE relaxation data were then used as the input for model-free analysis. The accurately extracted global tumbling parameters and the $R_1$, $R_2$, and NOE relaxation data were then used as the input for model-free analysis (*14*) to optimize the overall rotational diffusion model and the internal motional parameters for each spin. Five model-free parameter sets were iteratively tested and selected. The detailed fitting procedure was as described previously (*23*).

*Analysis of Hydrogen Exchange Data.* The intensities of the cross peaks in each 2D $^1H-^{15}N$ HSQC spectrum were

obtained to determine the H/D exchange rates. Rate constant ($k_{obs}$) of H/D exchange was calculated from a two-parameter nonlinear least-squares fit of the exponential decay curve to the equation (*26*)

$$I = I_o \exp(-k_{obs} t) + C \quad (1)$$

where $I$ represents the intensity of $^1H-^{15}N$ cross peaks in each 2D $^1H-^{15}N$ HSQC spectrum normalized to an external reference of *N-t*-BOC-glycine-U-$^{13}C_2$-$^{15}N$ (C I L, Inc.), which was contained in a capillary inside the NMR tube. $I_o$ is amplitude of the exchange decay curve. $k_{obs}$ is the measured exchange rate. $C$ is a constant.

As is well-known, under native conditions ($k_{cl} \gg k_{op}$), proton exchange can occur by EX1 ($k_{int} \gg k_{cl}$) and EX2 ($k_{cl} \gg k_{int}$) mechanisms. Here, the $k_{op}$, $k_{cl}$, and $k_{int}$ denote the opening, closing, and intrinsic rates of exchange, respectively. For proton exchange in a stable folded protein, the EX2 limit is almost always observed in the pH 4−7 (*27*), because formation of hydrogen-bonded structure is usually much faster than intrinsic exchange in proteins. The H/D exchange in [P62A]Ssh10b without denaturant at pH 4.8 is intrinsically slow for most of residues (see below), thus it is reasonable that the H/D exchange in [P62A]Ssh10b occurs by an EX2 mechanism. For [P62A]Ssh10b with denaturant GdmSCN, the highest concentration of GdmSCN used in the H/D exchange measurement is 2.0 M. Since the denaturant-induced unfolding process of [P62A]Ssh10b is started at about 1.5 M GdmSCN and the denaturant concentration at the midpoint of the transition is about 2.2 M (see the Supporting Information), the assumption that the H/D exchange in the presence of GdmSCN occurs by an EX2 mechanism is made for evaluating the changes in Gibbs free energy for opening hydrogen bonds ($\Delta G_{HX}$) which was calculated from equation

$$\Delta G_{HX} = -RT \ln(K_{op}) \quad (2)$$

where $R$ is the gas constant, $T$ is the absolute temperature, and $K_{op} = k_{obs}/k_{ex}$. The intrinsic exchange rate $k_{int}$ was from model peptides (*26*). Protection factor can be derived from the exchange rate constant $k_{obs}$ by the standard relation: $P = k_{int}/k_{obs}$ (*26, 28*). Both local fluctuations and global unfolding for opening reactions have be considered in the analysis of the denaturant dependence of the $\Delta G_{HX}$ data as described in the literature (*27, 29−31*).

## RESULTS

*Solution Structure of [P62A]Ssh10b.* Backbone and side-chain resonance assignments for [P62A]Ssh10b having 97 residues were obtained using standard triple-resonance experiments. The NMR-derived NOE distance restraints and dihedral angle and hydrogen bond information were used to calculate an ensemble structures. A superposition of the 20 lowest-energy structures of [P62A]Ssh10b is shown in Figure 1A. The structural statistics of the [P62A]Ssh10b ensemble are summarized in Table 1. The overall solution structure of [P62A]Ssh10b appears as a dimer that is almost identical to the X-ray structure of Alba except the loop regions (*7*) (see the Supporting Information, Figure 1).

[P62A]Ssh10b monomer consists of two α-helices ($\alpha_1$: 19−31 and $\alpha_2$:45−58) and one $\beta$-sheet as well as loops linking these secondary structural elements. The $\beta$-sheet is

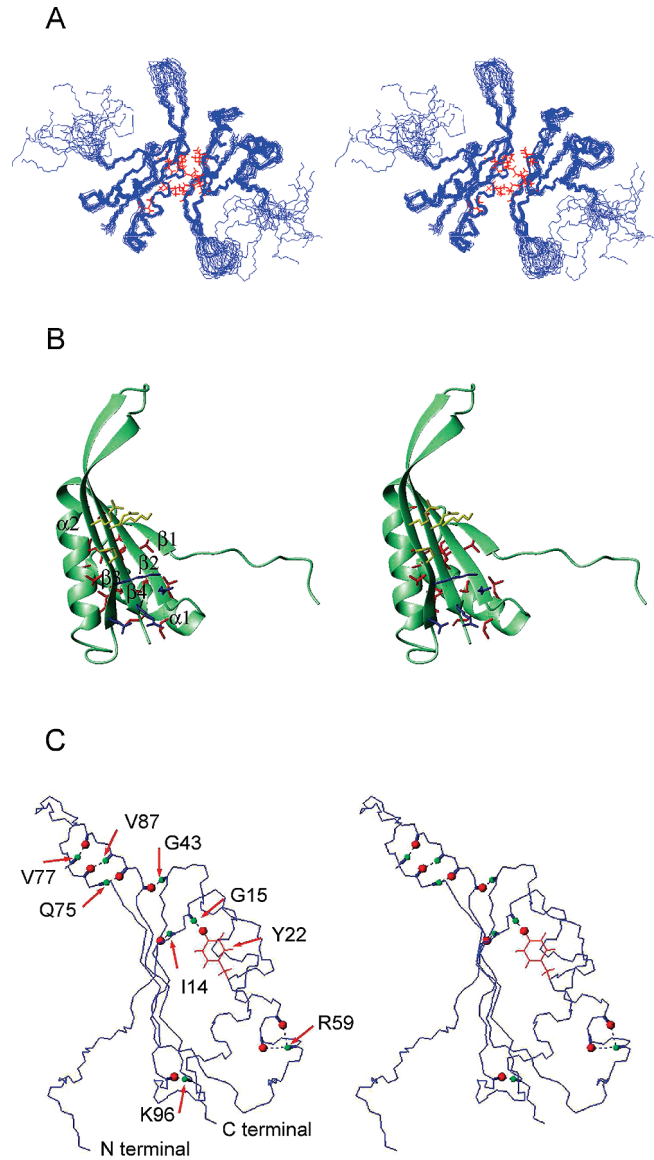


FIGURE 1: NMR-derived structure of [P62A]Ssh10b. (A) Stereoview of the 20 solution structures of [P62A]Ssh10b dimer. Side-chains of residues forming the hydrophobic cluster (red) in the dimer interface are shown. (B) Stereoview of the ribbon representation of [P62A]Ssh10b monomer, showing the packing of hydrophobic side-chains in the α/$\beta$-hydrophobic core and the ion-pair networks formed by polar residues in the $\beta$-sheet. The regular secondary structural elements are indicated. (C) The hydrogen bonds between residues in the loops and secondary structural elements. The oxygen and amide proton atoms are colored by red and green, respectively. Only the accepter residues are indicated in each pair of hydrogen bonds.

constructed by four $\beta$-strands ($\beta_1$:10−13, $\beta_2$:36−42, $\beta_3$: 66−73, and $\beta_4$:89−95). The strand $\beta_1$ is parallel to strand $\beta_2$, and strands $\beta_2$ and $\beta_3$ are antiparallel to strand $\beta_4$. Side-chains of the vast majority of hydrophobic residues in the $\beta$-sheet face to one side (hydrophobic side), and those of all hydrophilic residues face to solvent. Helices $\alpha_1$ and $\alpha_2$ are packed against the $\beta$-sheet on the hydrophobic side of the sheet. Residues V19, Y22, V23, A25, A26, L27, L29, and L30 in the helix $\alpha_1$, residues A45, A49, V53, I55, and V56 in the helix $\alpha_2$, and residues V12, I37, I39, A41, I92, and I94 in the $\beta$-sheet construct a hydrophobic core (α/$\beta$-hydrophobic core) (Figure 1B). Segment S74−S88 connecting strands $\beta_3$ and $\beta_4$ represents an extended $\beta$-hairpin loop

Table 1: Structural Statistics for the Family of 20 Structures of [P62A]Ssh10b

| | |
|---|---|
| rmsd from Idealized Covalent Geometry | |
| bonds (Å) | 0.0092 ± 0.0003 |
| angles (deg) | 1.07 ± 0.027 |
| ompropers | 0.98 ± 0.05 |
| rmsd from Experimental Restraints | |
| unambiguous distance restraints (Å) | 0.063 ± 0.016 |
| ambiguous distance restraints (Å) | 0.021 ± 0.003 |
| all distance restraints (Å) | 0.057 ± 0.014 |
| hydrogen bonds (Å) | 0.014 ± 0.004 |
| dihedral restraints (deg) | 0.15 ± 0.10 |
| Ramachandran Analysis (%) | |
| residues in most favorable regions | 86.6 |
| residues in additionally allowed regions | 12.0 |
| residues in generously allowed regions | 1.4 |
| residues in disallowed regions | 0 |
| Rmsd to Mean Structure | |
| backbone of secondary structure | 0.50 ± 0.08 |
| heavy atoms of secondary structure | 0.92 ± 0.10 |

($L_{\beta3\beta4}$) consisting of two antiparallel segments S74−S79 and R83-S88 and a regular β-turn ($\tau_1$) of residues Q80-R83. Residues G43 and R44 form a hinge linking strand $\beta_2$ and helix $\alpha_2$ ($L_{\beta2\alpha2}$). Loops $L_{\beta1\alpha1}$ (I14−P18), $L_{\alpha1\beta2}$ (Q32-S35), and $L_{\alpha2\beta3}$ (R59-I65) link the corresponding secondary structural elements in the monomer. As can be seen in Figure 1B, the monomer structure consists of two structural regions: one is a main body structural region including four β-strands and two α-helices as well as loops $L_{\beta1\alpha1}$, $L_{\alpha1\beta2}$, $L_{\beta2\alpha2}$, and $L_{\alpha2\beta3}$; the other is an extended β-hairpin loop $L_{\beta3\beta4}$.

The salt-bridges in [P62A]Ssh10b were identified using distance cutoffs of 4 and 6 Å. In the three antiparallel β-strands, residues K40−E91−R71 form a cross-strand ion-pair network and residue R71 in turn is salt-linked with E69 in the strand $\beta_3$. Because of a β-bulge in the strand $\beta_3$ around residue K68, a cross-strand ion-pair network is formed between residues K68−E36−R95−E66 (Figure 1B). A salt-bridge E54−R57 is formed in the helix $\alpha_2$.

In [P62A]Ssh10b dimer, residues I46, S47, V50, E54, R57, and N58 of helix $\alpha_2$; I67, I70, V72, and G73 of strand $\beta_3$; I90 and I92 of strand $\beta_4$; and S74, R86, and S88 of β-hairpin loop are involved in the dimer interface. A cluster of hydrophobic residues I46, V50, I67, I70, V72, and I90 is at the middle of the dimer interface (Figure 1A).

*Hydrogen Exchange in the Absence and Presence of GdmSCN.* The stability of [P62A]Ssh10b to breaking of hydrogen bond was probed by H/D exchange in the absence and presence of a very strong denaturant GdmSCN (*32*). A series of 2D $^1H-^{15}N$ HSQC spectra were recorded for [P62A]Ssh10b at 310 K in the presence of 0−2.0 M concentrations of GdmSCN. Compared to the assignment of amide proton ($^1H_N$) resonances in the spectrum of [P62A]Ssh10b (*10*), assignment of resonance signals in the 2D $^1H-^{15}N$ HSQC spectra of [P62A]Ssh10b in GdmSCN was straightforward because of the gradual shift of the signals with increasing GdmSCN concentration from 0 to 2.0 M.

The 2D $^1H-^{15}N$ HSQC spectrum of [P62A]Ssh10b in $H_2O$ shows cross peaks for 91 residues (see the Supporting Information, Figure 2A), because there are three prolines (P6, P8, and P18) in the protein and cross peaks for residues M1−S3 are missing. The 2D $^1H-^{15}N$ HSQC spectrum of freshly dissolved [P62A]Ssh10b in $D_2O$ provided cross peaks for 54 amide groups (60% of the 91 residues) which can be used as site-specific probes in the H/D exchange measurements (see the Supporting Information, Figure 2B). $^1H_N$ of 37 residues exchanged too rapidly to record in the first spectrum of measurements. Segment of the first nine residues is disordered, and no protection is imposed on $^1H_N$ of residues G4-T5, T7, S9−N10 to prevent solvent exchange. $^1H_N$ of residues K16−K17, Q32−S35, R44, F60-D63, I65, S74, V76, and T78−R86 in loops have no protection from solvent exchange. $^1H_N$ of E36 from strand $\beta_2$ and I67, I70, and V72 from strand $\beta_3$ are not involved in cross-strand hydrogen bonds. Residues V19−N21, A45, and S47 are in the N-terminal regions of helices $\alpha_1$ and $\alpha_2$, which are not involved in $^1H_{Ni}-O_{i-4}$ hydrogen bonds in helix. Hydrogen exchange profiles for the 54 protected amide groups are provided in Figure 2A−C. Twenty-two of the 54 amide groups provided the profiles represented by almost flat lines. Five of the 54 amide groups showed very slightly decayed curves. The resonance signals of these 27 amide groups remained in the 2D HSQC spectrum acquired after 60 h of dissolving the protein in $D_2O$ (see the Supporting Information, Figure 2C), and more than 90% of the initial intensity remained even after 115 h (see the Supporting Information, panels D and E in Figure 2). These 27 amide protons are named nonexchangeable amide protons in [P62A]Ssh10b. Their protection factors are unable to calculate. On the other hand, the other 27 of 54 amide groups showed a decrease to zero in peak intensity after 60 h, for which the protection factors were obtained under native conditions (Figure 2D).

The amide protons of 54 residues can be classified into three groups according to their relative protection factors. Group 1 includes all the nonexchangeable amide protons which are 22 amide protons persisted in $D_2O$ over 300 h and amide protons showing a slightly linear decreasing of intensity: $^1H_N$ of V12, L24, I37, A49, and T89 in the β-strands and α-helices (Figure 2A, D, and E). The 22 persisted amide protons are $^1H_N$ of V23, A26−L27, and L29−L30 in the helix $\alpha_1$; V50−V56 in the helix $\alpha_2$; V38−A41 in the strand $\beta_2$; and I90−R95 in the strand $\beta_4$. $^1H_N$ of I90−R95 in the strand $\beta_4$ are hydrogen bonded to strands $\beta_3$ and $\beta_2$ on both sides, in turn $^1H_N$ of I39 and A41 and $^1H_N$ of V38 and K40 in the strand $\beta_2$ are hydrogen bonded to the strands $\beta_4$ and $\beta_1$, respectively. In this case, the protection factors can be only arbitrary estimating to be higher than $2.0 \times 10^6$. Group 2 includes amide protons of I14, Y22, A25, T28, N31, G43, I46, K48, R57, N58, E66, R71, G73, Q75, V77, V87, and K96 giving exponential exchange profiles (Figure 2B−E). The protection factors for these amide protons are in the range of $1.6 \times 10^4$ to $2.0 \times 10^5$. The amide protons of T28, R57, E66, and R71 in this group participate in the hydrogen bonds in regular secondary structures. Most of the rest residues in this group are located in the joining regions between loops and regular secondary structures. Among them $^1H_N$ of Q75, V77, and V87 (Figure 2C−E) may form hydrogen bonds between the antiparallel segments of the extended β-hairpin loop. Group 3 comprises weakly protected amide protons: $^1H_N$ of L13, G15, R42, K64, K68, E69, S88, and K97, which exhibit very fast solvent exchange with protection factors in the range of 120 to $6.0 \times 10^3$ (Figure 2C−E). The $^1H_N$ of these residues may participate in very weak hydrogen bonds, and most of these

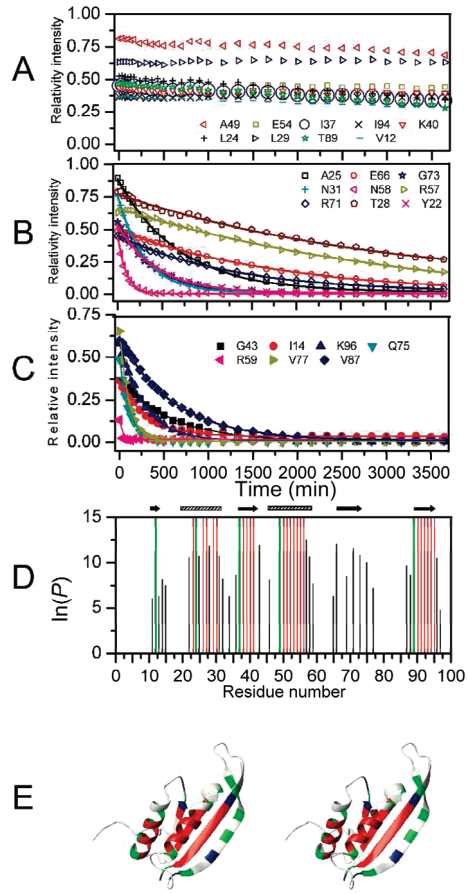


FIGURE 2: Hydrogen exchange results of [P62A]Ssh10b under native conditions (0 M GdmSCN). (A) Hydrogen exchange profiles for highly protected amide protons of representative residues in group 1. (B) Hydrogen exchange profiles of residues in groups 2 and 3. (C) Hydrogen exchange profiles of residues in loops. Continuous lines show the best fits to a single-exponential function. (D) Protection factors plotted against residue number. The protection factors of the strongly protected amide protons in group 1 are unable to calculate, and therefore indicated by full scale of ln(*P*) (arbitrarily set to 15 based on the highest calculated value of ~12.5 for residues in the other groups) red and green bars: red bars, amide protons persisted in $D_2O$; green bars, five amide protons exhibiting very slowly solvent exchange (the estimated protection factor to be $>2.0 \times 10^6$). The black bars indicate the protection factors for other residues showing exponential exchange profiles. (E) Mapping the residues on the monomer structure, amide protons of which are grouped by three types of opening reactions. The backbone is colored by red, green, and blue for group 1, 2, and 3, respectively.

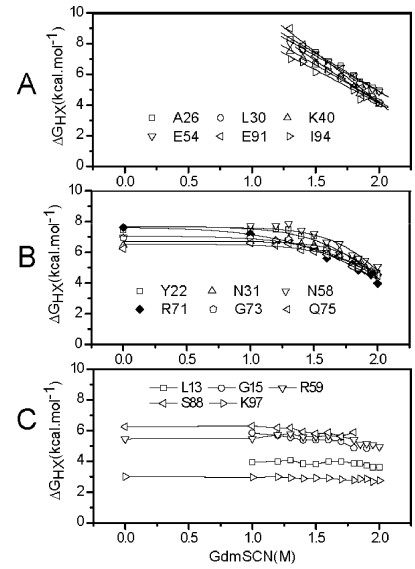


FIGURE 3: Free energy of hydrogen exchange ($\Delta G_{HX}$) as a function of [GdmSCN] for 17 representative residues of [P62A]Ssh10b. (A) Amide protons having protection factors $>2.0 \times 10^6$ show the strong dependence on denaturant at higher [GdmSCN]. (B) Amide protons having protection factors range from $1.6 \times 10^4$ to $2.0 \times 10^5$ show weak dependence on denaturant at low [GdmSCN] and strong dependence at high [GdmSCN]. (C) Amide protons having protection factors in the range of 120 to $6.0 \times 10^3$ showing weak dependence on GdmSCN concentrations.

residues are located in loops $L_{\beta1\alpha1}$, $L_{\beta2\alpha2}$, and $L_{\alpha2\beta3}$. K68 and E69 are two residues at the $\beta$-bulge in the strand $\beta_3$. The relatively weak protection for $^1H_N$ of residues E66, R71, and G73 in the strand $\beta_3$ is probably due to the $\beta$-bulge around residue K68.

The above-mentioned 54 amide protons can be subjected to detect the GdmSCN concentration ([GdmSCN]) dependence of H/D exchange. Figure 3 shows the obtained free energy of hydrogen exchange ($\Delta G_{HX}$) as a function of [GdmSCN]. For $^1H_N$ of the residues in group 1, a significant linear decrease of $\Delta G_{HX}$ with increasing of [GdmSCN] was obtained at [GdmSCN] $\geq$ 1.4 M (Figures 3A and 2E). The dominant contributions to solvent exchange of these residues are from global unfolding reactions, since expose a large amount of new surface to denaturant will be promoted with increasing concentration of denaturant under this mechanism (*29*). $\Delta G_{HX}$ for residues in group 2 is initially invariant at low [GdmSCN] and increases at high [GdmSCN] (Figures 3B and 2E). In this case, $\Delta G_{HX}$ is modeled to contain contributions from mixed exchange mechanism. At low [GdmSCN], the exchange is primarily associated with local fluctuations, while at higher [GdmSCN], the dependence of exchange on denaturant increases dramatically, indicating a "global" opening reaction. The solvent exchange for residues in group 3 is dominated by local fluctuations, showing a slightly linear decrease in $\Delta G_{HX}$ with increasing GdmSCN over the whole range of denaturant concentrations (Figures 3C and 2E), because the localized noncooperative opening reaction will show little dependence on denaturant concentration (*29*). Therefore, three types of opening reactions can be characterized by the obtained [GdmSCN] dependence of $\Delta G_{HX}$, which contributes to solvent exchange of 54 residues. The first involves cooperative unfolding reactions (global unfolding reaction) at higher [GdmSCN], contributing to H/D exchange of 50% of 54 residues. The second involves local fluctuations at low [GdmSCN] and partial or complete unfolding reactions at higher [GdmSCN] (solvent exchange through combination of local structure fluctuations and global unfolding process, we simply call it as combined unfolding process hereafter), contributing to H/D exchange of 31.5% of 54 residues. The third involves solvent exchange through local fluctuations over the whole range of [GdmSCN], which can be identified only for 18.5% of 54 residues.

The $\Delta G_{u,HX}(H_2O)$ representing the free energy for opening hydrogen bonds through the unfolding reactions and $m_{HX}$ parameters were obtained by the nonlinear least-squares fitting of the $\Delta G_{HX}$ derived from amide H/D exchange measurements (*26*−*29*). Figure 4 shows that residues in the two α-helices and four $\beta$-strands have the higher $\Delta G_{u,HX}(H_2O)$ and $m_{HX}$ values than the residues in the other structural regions of the protein. Moreover, residues in group

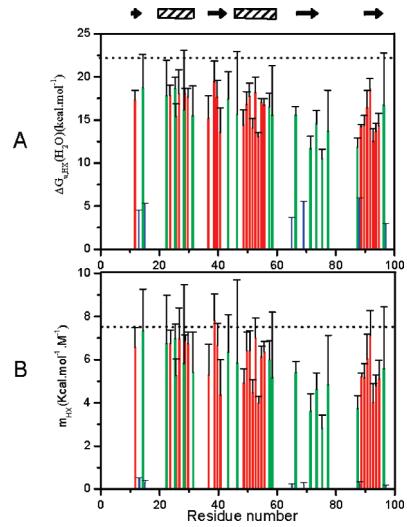


FIGURE 4: Sequence dependence of thermodynamic parameters estimated from H/D exchange. (A) $\Delta G_{u,HX}(H_2O)$ and (B) $m_{HX}$ values obtained from nonlinear least-squares fits of the GdmSCN concentration dependence of $\Delta G_{HX}$. Color code: red bars, amide protons that exchange through global unfolding at [GdmSCN] > 1.4 M; green bars, amide protons that exchange through combination of local structure fluctuations and global unfolding; blue bars, amide protons that exchange through local fluctuation. Doted horizontal lines depict $\Delta G_u(H_2O)$ and *m*-value for [P62A]Ssh10b estimated from equilibrium unfolding experiments.

1 have the highest $\Delta G_{u,HX}(H_2O)$ and $m_{HX}$ values, which are about 18.1 kcal/mol and 7.1 kcal mol$^{-1}$ M$^{-1}$, respectively. On the other hand, the fluorescence measurements provided the $\Delta G_u(H_2O)$ value of ~22.2 kcal/mol and the magnitude of the slope about 7.5 kcal mol$^{-1}$ M$^{-1}$ (see the Supporting Information, Figure 3A). Actually, the H/D exchange for a protein with stability of $\Delta G_u(H_2O) = 22.2$ kcal/mol should take a very long time to observe decay of peak intensities, and the decay of such peak intensities is expected to be essentially a flat line. This was indeed observed for residues in group 1, indicating the consistent with the value 22.2 kcal/mol. However, the lower $\Delta G_{u,HX}(H_2O)$ value of 18.1 kcal/mol was obtained for residues in group 1. Such a discrepancy between $\Delta G_{u,HX}(H_2O)$ and $\Delta G_u(H_2O)$ has been also observed in other proteins, and was proposed that $\Delta G_{HX}$, measured at mild conditions, would appear lower than $\Delta G_u(H_2O)$, measured under more severe conditions through the transition region (*27*). The H/D exchange measurement in the presence of GdmSCN in this study was not under conditions through the transition region of unfolding. The above analysis suggests that packing of two α-helices and four β-strands in the main body structural region constructs a highly stable α/β-hydrophobic core in the [P62A]Ssh10b monomer in terms of the localized hydrogen-bond breaking motions (Figure 2E).

*Backbone Dynamics of [P62A]Ssh10b and [K40N/P62A]Ssh10b.* The relaxation parameters $R_1$, $R_2$ and $^1H-^{15}N$ NOE, were measured for both [P62A]Ssh10b and [K40N/P62A]Ssh10b (Figure 5) for investigating the differences in internal motions between two proteins having different thermal stability. Substitution of K40 with N40 caused a decrease in thermostability of [K40N/P62A]Ssh10b. The $\Delta G_u(H_2O)$ and melting temperature $T_m$ of [K40N/P62A]Ssh10b decreased 3.1 kcal/mol and 20 °C, respectively compared to those of [P62A]Ssh10b (see the Supporting Information, Figure 4 and Table 1). However, the 2D $^1H-^{15}N$ HSQC spectrum of [K40N/P62A]Ssh10b is very similar to the spectrum of [P62A]Ssh10b (see the Supporting Information, Figure 5A), and the significant shift of the cross peaks can be observed only for residues involving in the ion pair network K40−E91−R71−E69 and in region around residue I14 which is hydrogen bonded to K40 (see the Supporting Information, Figure 5B). Thus, K40N mutation destabilizes significantly the mutant protein while the nativelike structure remains. The destabilized [K40N/P62A]Ssh10b is predominantly in the folded state under the NMR experimental condition.

Figure 5 shows the $^1H-^{15}N$ NOE data for both the [P62A]Ssh10b and [K40N/P62A]Ssh10b, which reflect primarily high-frequency (ps−ns time scale) local backbone motions of the proteins. [K40N/P62A]Ssh10b provides very similar but somewhat smaller $^1H-^{15}N$ NOE values compared to [P62A]Ssh10b. The N- and C-terminal residues G4−N10 and K97, respectively, and residues V77−R86 in loop $L_{\beta3\beta4}$ showed reduced $^1H-^{15}N$ NOE values (<0.6), characterizing the backbone flexibility of these residues on ps−ns time scale. Great majority residues in loop $L_{\alpha2\beta3}$ and residues G33 and S35 in loop $L_{\alpha1\beta2}$ have $^1H-^{15}N$ NOE values >0.6, showing restricted local motions of these regions. The residues in ordinary secondary structural elements (except residue E69 in strand $\beta_3$) and loop $L_{\beta1\alpha1}$ and hinge $L_{\beta2\alpha2}$ have higher $^1H-^{15}N$ NOE values (>0.7), reflecting the highly restricted ps−ns motions of these regions. The overall $R_1$ and $R_2$ values of [P62A]Ssh10b are remarkably smaller and larger, respectively, than those of [K40N/P62A]Ssh10b. The $R_2$ values of residues in secondary structural regions of [K40N/P62A]Ssh10b decrease ~1.2-fold compared to those of [P62A]Ssh10b. The average $R_2/R_1$ ratio is 16.9 ± 1.2 (calculated for 48 residues) for [P62A]Ssh10b and 14.2 ± 1.0 (calculated for 54 residues) for [K40N/P62A]Ssh10b (Figure 5 and the Supporting Information, Table 2). Apparently, the relaxation parameters reveal relatively less restricted backbone motions of [K40N/P62A]Ssh10b compared to [P62A]Ssh10b.

The relaxation data were analyzed for individual residues of both proteins by the Liparli-Szabo approach (*31*). The determined correlation times for overall rotational motion ($\tau_m$) and axially symmetric diffusion tensor components and the angles ($\theta$ and $\varphi$) for both proteins are listed in Table 2. The smaller global tumbling times of [K40N/P62A]Ssh10b than those of [P62A]Ssh10b likely arise from differences in their hydration properties, as observed for other proteins (*33*).

The model-free parameters $S^2$, $\tau_e$, and $R_{ex}$ obtained for both proteins are shown in Figure 5. The general order parameter $S^2$ for residues in two α-helices and four β-strands as well as $L_{\beta1\alpha1}$ and $L_{\beta2\alpha2}$ of both proteins have higher values (>0.8). The average $S^2$ value for two α-helices and four β-strands of [P62A]Ssh10b is 0.91 ± 0.04, which is slightly higher than that obtained for [K40N/P62A]Ssh10b having a value of 0.87 ± 0.03. Moreover, both proteins have similar average $S^2$ values for loops $L_{\beta1\alpha1}$ and $L_{\alpha1\beta2}$, but different $S^2$ values for loop $L_{\alpha2\beta3}$ and long β-hairpin loop $L_{\beta3\beta4}$. [P62A]Ssh10b gives average $S^2$ value of 0.91 ± 0.03 for loop $L_{\alpha2\beta3}$, but smaller value of 0.83 ± 0.03 was obtained for [K40N/P62A]Ssh10b. These data suggest that [P62A]Ssh10b has a relatively compact main body structure of lower flexibility compared to [K40N/P62A]Ssh10b. The $S^2$ values for residues

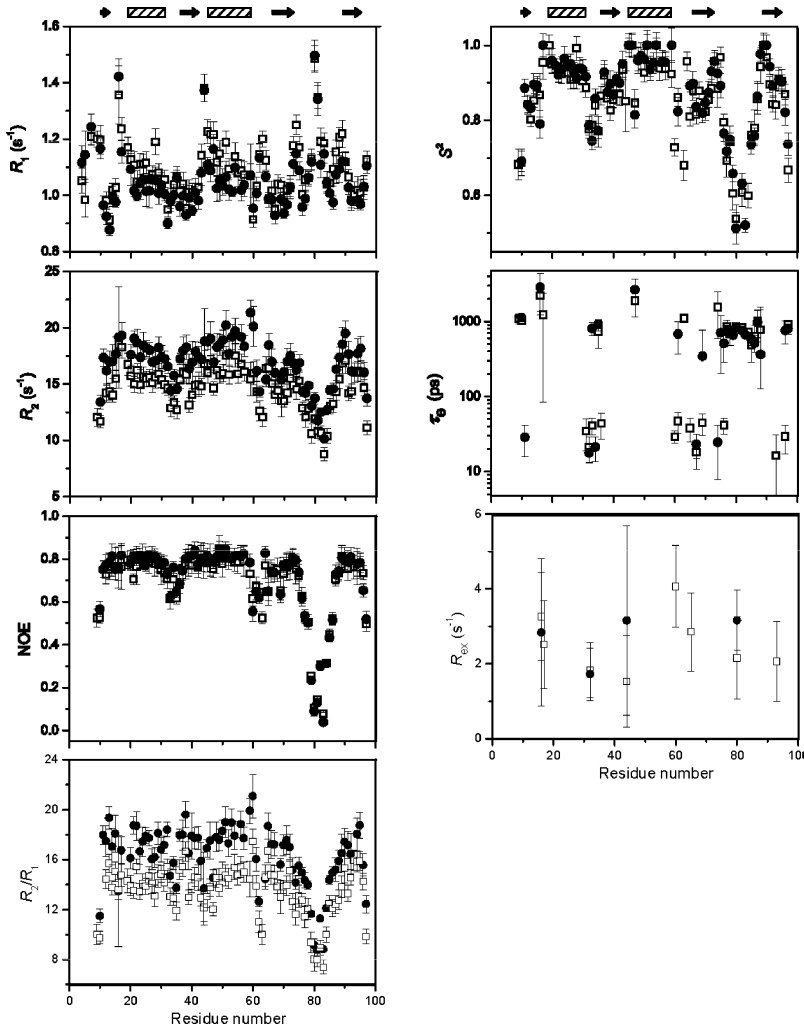


FIGURE 5: $^1H-^{15}N$ NMR relaxation and model-free parameters for [P62A]Ssh10b (•) and K40N mutant [P62A]Ssh10b (□). $R_1$, $R_2$, $^1H-^{15}N$ NOE, order parameter $S^2$, internal effective correlation time $\tau_e$, and parameter for slow conformational exchange motions $R_{ex}$ were plotted against residue number.

Table 2: Global Tumbling Dynamic Parameters Optimized from Model-Free Analysis

| | [P62A]Ssh10b | [K40N/P62A]Ssh10b |
|---|---|---|
| $\tau_m$ (ns) | 12.972 ± 0.048 | 11.703 ± 0.044 |
| $D_\parallel/D_\perp$ | 0.864 ± 0.024 | 0.882 ± 0.022 |
| $\theta$ (deg) | −123.13 ± 7.06 | 122.47 ± 8.42 |
| $\varphi$ (deg) | 104.78 ± 7.63 | −68.95 ± 8.90 |

in loop $L_{\beta3\beta4}$ of both proteins decreased toward the $\beta$-turn region (Q80-R83), varying from 0.98 ± 0.02 to 0.51 ± 0.04 in [P62A]Ssh10b and from 0.97 ± 0.03 to 0.53 ± 0.04 in [K40N/P62A]Ssh10b. Residues S74, Q75, V87, and S88 in both terminal regions of this loop have similar higher average $S^2$ value (~0.91), whereas segment S79−Q84 of the loop gives lower average $S^2$ value about 0.59 for both proteins, enriched in ps−ns internal motions. Thus, a rigid to completely flexible transition occurred in the loop $L_{\beta3\beta4}$ of both proteins. The high $\tau_e$ values were obtained mainly for residues in the loop regions of both proteins. No conformational exchange motions can be detected for contiguous residues in both proteins (Figure 5). Therefore, the dynamic structure of [P62A]Ssh10b as well as [K40N/P62A]Ssh10b monomers can be divided to two structural regions which are coincident with the two structural regions in the NMR-derived solution structure. One is the main body structural region containing α/$\beta$-hydrophobic core, the high compactness of which is evident in its high $S^2$ values and absence of $R_{ex}$ contributions. The other is the extended $\beta$-hairpin loop $L_{\beta3\beta4}$, exhibiting the rigid to flexible transitions.

In consequence, the backbone dynamic studies of [P62A]-Ssh10b and its K40N mutant protein reveal that [K40N/P62A]Ssh10b has relatively less restricted backbone motions exhibiting a relatively less compact structure of higher flexibility compared to [P62A]Ssh10b.

## DISCUSSION

[P62A]Ssh10b is a homodimeric protein. The dimeric interactions between the two subunits are mediated predominantly by the hydrophobic contacts involving side-chains of residues I46, V50, I67, I70, V72, and I90 from both monomeric subunits (Figure 1A). [P62A]Ssh10b showed a two-state denaturation curve which is validated by a latest report (*34*). This means no preglobal unfolding is detected in the denaturation experiments, implying the concerted folding and dimerization of [P62A]Ssh10b. The highly cooperatively folding/unfolding of [P62A]Ssh10b is also suggested by the native-hydrogen exchange data. From these inferences, all the following analysis of structural basis of thermostability is related to the monomer motif of [P62A]Ssh10b.

*The Stabilizing α/β-Hydrophobic Core of [P62A]Ssh10b.* For [P62A]Ssh10b, the tertiary hydrophobic packing interactions between side-chains of 19 hydrophobic residues in the α/β-hydrophobic core and hydrogen-bonding interactions between residues of adjacent strands in the β-sheet and between $^1H_N$ and C═O of *i*th and (*i*−4)th residues, respectively, in the α-helix are the key factors contributing to the stability of the α/β-hydrophobic core. In addition, some cross-segment hydrogen bonds were formed between the loops and other secondary structural elements in the main body structural region of [P62A]Ssh10b monomer. The hydrogen bonds of residues in the loops $L_{\beta1\alpha1}$ and $L_{\alpha1\beta2}$ and hinge $L_{\beta2\alpha2}$ with residues in the β-strands can be identified according to the degree of protection from solvent exchange and to geometric criteria of hydrogen bond (Figures 1C and 2D). $^1H_N$ of I14 in loop $L_{\beta1\alpha1}$ is hydrogen bonded to C═O of K40 in the strand $\beta_2$. $^1H_N$ of G43 in hinge $L_{\beta2\alpha2}$ is hydrogen bonded to C═O of S88 which is a terminal residue in the extended β-hairpin loop ($L_{\beta3\beta4}$) connecting directly to strand $\beta_4$. In turn, S88 is located in the antiparallel N- and C-terminal portions of loop $L_{\beta3\beta4}$ stabilized by the cross-strand hydrogen bonds: V77 $^1H_N$−S85 C═O, Q75 $^1H_N$−V87 C═O, and Q75 C═O−V87 $^1H_N$. Moreover, one cross-segment hydrogen bond S35 C═O−K96 $^1H_N$ between $L_{\alpha1\beta2}$ and the C-terminal end of the strand $\beta_4$ was formed. These cross-segment hydrogen-bonds (Figure 1C) may also make important contributions to the tight packing of two α-helices against the β-sheet in [P62A]Ssh10b.

In fact, the high $S^2$ values (>0.8) and absence of conformational exchange motions of the β-sheet and two α-helices from backbone dynamic measurements indicate a compact structure of α/β-hydrophobic core in [P62A]Ssh10b. On the other hand, the vast majority residues in the β-strands and α-helices as well as above-mentioned residues I14, G43, Q75, V77, V87, and K96 in the loops have highly protected amide protons which exchange with solvent by means of a global or combined unfolding process. Moreover, these residues have the values of $\Delta G_{u,HX}(H_2O)$ approaching those of the equilibrium $\Delta G_u(H_2O)$ (Figure 4). These data suggest strongly the high conformational stability of the compact α/β-hydrophobic core in [P62A]Ssh10b. Thus, the α/β-hydrophobic core behaviors as a "stabilizing core" in [P62A]Ssh10b.

The K40N mutation of [P62A]Ssh10b greatly decreases the thermostability of the mutant protein (see the Supporting Information, Table 1). The significant increase in H/D exchange rates of all the residues in above classified group 1 was observed for [K40N/P62A]Ssh10b (data will be published elsewhere). Meanwhile, [K40N/P62A]Ssh10b has a less-compact structure with relatively high flexibility. The loop $L_{\alpha2\beta3}$ linking helix $\alpha_2$ and strand $\beta_3$ in the α/β-hydrophobic core is more flexible in [K40N/P62A]Ssh10b than that in [P62A]Ssh10b. These data collectively suggest that the K40N mutation may disturb the packing of helix against the β-sheet in the mutant [P62A]Ssh10b reducing the stability of the α/β-hydrophobic core.

The dynamic properties of [P62A]Ssh10b display rigid body movement of the segments in the regular secondary structures with no substantial conformational exchange contributions characterized by $R_{ex}$ values (Figure 5). Only residues K16, R44, and Q80 show the $R_{ex}$ contributions ($R_{ex} \geq 2.7$ Hz). The $S^2$ values of K16 (∼0.79), R44 (∼0.83), and Q80 (∼0.50) are relatively lower than their flanking residues.

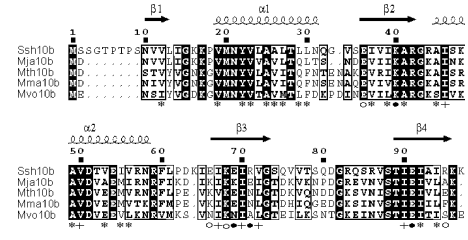


FIGURE 6: Sequences alignment of archaeal Ssh10b homologues using ENDscript. Mja10b, Mth10b, Mma10b, and Mvo10b are from *Methanococcus jannaschii*, *Methanococcus thermolithotrophicus*, *Methanococcus maripaludis*, and *Methanococcus voltae*, respectively. Residues with side-chains involved in formation of hydrophobic core (*) and hydrophobic cluster in the dimer interface (+) are indicated on the basis of the structure of [P62A]Ssh10b. The residues form two ion-salt networks are distinguished by solid and open circle marks.

Interestingly, K16 undergoes deacetylation by Sir2 that affects the DNA-binding affinity of Alba (*2*). K16, R44, and Q80 are involved in the interactions of [P62A]Ssh10b dimer with DNA (*10*). The structure region of central "belly" having K16 and R44 and the β-turn containing Q80 of loop $L_{\beta3\beta4}$ were supposed to form a potential DNA-binding site in the [P62A]Ssh10b dimer (*2, 10*). K16 and R44 are located in the main body structural region and Q80 is at the flexible turn of the extended β-hairpin loop $L_{\beta3\beta4}$. Thus, the stabilizing α/β-hydrophobic core region in the main body of monomer must be of great importance to the biological function of [P62A]Ssh10b.

*Hydrophobic Interactions Are a Major Determinant for Thermal Stability of [P62A]Ssh10b.* The heat-induced unfolding experiments of [P62A]Ssh10b (see the Supporting Information, Figure 3B) provided the melting temperature ($T_m$=395.6 ± 2.1 K) and enthalpy of unfolding at melting temperature ($\Delta H_m$=143.1 ± 3.1 kcal/mol) see the Supporting Information, Figure 3C), which are fairly close to the values obtained for Ssh10b (*8*). The mesophilic or thermophilic counterpart proteins, archaeal Mja10b, Mth10b, Mma10b, and Mvo10b, were isolated from *Methanococcus jannaschii*, *Methanococcus thermolithotrophicus*, *Methanococcus maripaludis*, and *Methanococcus voltae*, respectively, which have optimum growth temperatures of 85, 65, 35, and 35 °C, respectively. Archaeal Mja10b, Mth10b, Mma10b, and Mvo10b are members of the Sac10b family. Lacking of knowledge of any mesophilic counterpart protein structure, the approach of sequence comparison is used in the analysis. Secondary-Structure-Driven sequence alignment, using the ENDscript web server (*35*) and the structure of [P62A]Ssh10b as an aid in determining gap positions, showed that Mja10b, Mth10b, Mma10b, and Mvo10b share a high degree of similarity in both secondary structures and amino acid sequences with Ssh10b isolated from *Sulfolobus shibatae* having optimum growth temperature of 85 °C (Figure 6). Because Mja10b, Mth10b, Mma10b, and Mvo10b have about 30% sequence identity and 78% similarity with Ssh10b, the majority residues comprising the α/β-hydrophobic core of [P62A]Ssh10b are conserved between the Ssh10b and four archaeal proteins. Besides, the majority of nonconserved residues are also hydrophobic. Presumably, a similar α/β-hydrophobic core could exist in Mja10b, Mth10b, Mma10b, and Mvo10b. However, there is an exception to the hydrophobicity of amino acids at positions 29, 45, and 53 (Figure 6). Mja10b, Mth10b, and Mma10b have Q29 instead of L29,

Table 3: Comparison of Mean Generalized Order Parameters ($\langle S^2 \rangle$) of Secondary Structural Elements in [P62A]Ssh10b and [K40N/P62A]Ssh10b

| | mean generalized order parameters ($\langle S^2 \rangle$) | |
|---|---|---|
| secondary structure | [P62A]Ssh10b | [K40N/P62A]Ssh10b |
| $\beta_1$ | $0.81 \pm 0.05$ | $0.78 \pm 0.04$ |
| $\alpha_1$ | $0.94 \pm 0.02$ | $0.92 \pm 0.02$ |
| $\beta_2$ | $0.90 \pm 0.01$ | $0.86 \pm 0.02$ |
| $\alpha_2$ | $0.97 \pm 0.03$ | $0.94 \pm 0.02$ |
| $\beta_3$ | $0.89 \pm 0.05$ | $0.86 \pm 0.02$ |
| $\beta_4$ | $0.94 \pm 0.05$ | $0.90 \pm 0.04$ |

which is located on the C-terminal region of helix $\alpha_1$ in [P62A]Ssh10b (Figure 6). This does not seem to influence the stabilities of archaeal proteins since Mja10b is as stable as Ssh10b and has same dimeric fold as [P62A]Ssh10b (*36*). Mvo10b and Mma10b are all mesophilic proteins. Mvo10b has L29 in the sequence, but has S45 instead of A45 on the N-terminus of helix $\alpha_2$. However, Mvo10b shows same thermal stability to Mma10b which has A45 in the sequence (Figure 6). Thus, nonconserved residue at sequence position 45 may not be critical for the thermostability of these archaeal proteins. [P62A]Ssh10b has a V53, the side chain of V53 points to the inside of the $\alpha/\beta$-hydrophobic core (see the Supporting Information, Figure 6), and Mja10b has an alanine at position 53 (Figure 6). However, Mth10b, Mma10b, and Mvo10b have no hydrophobic amino acid at position 53, but a hydrophilic E53 (Figure 6). This raises a question whether E53 is a residue influencing the thermostability of Mth10b, Mma10b, and Mvo10b compared to those of [P62A]Ssh10b. For clarifying the influence of residue at position 53 on thermostability of the protein, the V53E mutant [P62A]Ssh10b was isolated and subjected to the denaturant-induced and heat-induced unfolding experiments (see the Supporting Information, Figure 4 and Table 1). The results have shown that the $C_{mid}$ value for V53E mutant [P62A]Ssh10b is 3.16 much lower than those for [P62A]Ssh10b ($C_{mid} = 4.09$). The difference in the $\Delta G_u(H_2O)$ values and melting temperatures between V53E mutant [P62A]Ssh10b and [P62A]Ssh10b is 4.8 (kcal/mol) and 40 °C, respectively. Apparently, the substitution of E53 for V53 in [P62A]Ssh10b molecule disturbs severely the compact packing arrangement of the hydrophobic side-chains, consequently reduces the conformational stability of the $\alpha/\beta$-hydrophobic core. Thus, the V53E mutation destabilizes the [P62A]Ssh10b by altering the hydrophobic interaction in the $\alpha/\beta$-hydrophobic core of V53E mutant [P62A]Ssh10b. On the other hand, the denaturant-induced and heat-induced unfolding experiments of Mvo10b showed unfolding at lower denaturant concentrations providing the lower $\Delta G_u(H_2O)$ value than the value obtained for [P62A]Ssh10b (data will be reported elsewhere). Therefore, the above sequence comparison and mutagenesis results suggest that hydrophobic interactions and packing compactness within the $\alpha/\beta$-hydrophobic core can be proposed to be a basis for thermal stability of [P62A]Ssh10b. Presumably, the thermostability of [P62A]Ssh10b is interrelated to the stabilizing $\alpha/\beta$-hydrophobic core.

It was confirmed that protein thermostability is reached through diverse stabilizing interactions (*37*). Many factors, including the packing efficiency through hydrophobic interactions, ion pairs, and/or hydrogen bonds contributions, and the stabilization of loops, have been assumed to be responsible for protein thermal stabilization (*38, 39*). In addition, the increase of conformational rigidity has been observed in many thermophilic and hyperthermophilic proteins, and the link between conformational rigidity and hyperthermostability has been addressed (*40, 41*). In fact, many hyperthermostable proteins show high conformational rigidity, but there are also exceptions to this stability/rigidity link. The question whether the core region of [P62A]Ssh10b has high conformational rigidity can be clarified by comparing to the relaxation data of mesophilic counterpart of [P62A]Ssh10b, which is currently undertaken.

As was proposed, the increased presence of ion pairs confers thermal stability due to the significantly reduced desolvation penalty for ion-pair formation at increased temperatures (*42*). An increase of ion pairs and ion-pair networks in particular is a common phenomenon observed in hyperthermostable proteins. This observation can support the proposal that electrostatic interactions are an important factor conferring thermostability to proteins; however, conflicting conclusions also exist. It should be mentioned that [P62A]Ssh10b has two ion-pair networks involving K40−E91−R71−E69 and K68−E36−R95−E66 on solvent-accessible surface of the $\beta$-sheet and a salt-bridge E54−R57 in the helix $\alpha_2$, which have been identified in both X-ray structure of Sso10b and solution structure of [P62A]Ssh10b. Residues E36, K40, K68, and E91 as well as E54 are conserved across the above-mentioned thermophilic and mesophilic archaeal proteins. What role the ionization interactions playing in the thermostability of [P62A]Ssh10b could not be predicted just by sequence comparison and structural analysis. For detailed studies of the contribution of salt bridges, various mutations targeted to the ionizable residues have been constructed and the thermodynamic characterization is currently undertaken.

In conclusion, the above-described structural and dynamic as well as thermodynamic characteristics of the protein suggest strongly that the hydrophobic interactions in cooperation with hydrogen bonding interactions are the major determinant for the thermostability of the thermophilic [P62A]Ssh10b. Thus, the thermostability of [P62A]Ssh10b may be correlated with the stabilizing $\alpha/\beta$-hydrophobic core having a compact structure.

## ACKNOWLEDGMENT

We thank Professor William B. Whitman (Department of Microbiology, University of Georgia) for providing the sequences of archaeal Mth10b, Mma10b, and Mvo10b.

## SUPPORTING INFORMATION AVAILABLE

Six figures and two tables are shown, providing the additional data for H/D exchange of [P62A]Ssh10b and denaturant- and heat-induced unfolding of [P62A]Ssh10b and its K40N- and V53E mutant proteins (PDF). This material is available free of charge via the Internet at http://pubs.acs.org.

## REFERENCES

1. Grote, M., Dijk, J., and Reinhardt, R. (1986) Ribosomal and DNA binding proteins of the thermoacidophilic archaebacterium Sulfolobus acidocaldarius. *Biochim. Biophys. Acta 873*, 405–413.
2. Bell, S. D., Botting, C. H., Wardleworth, B. N., Jackson, S. P., and White, M. F. (2002) The interaction of Alba, a conserved

archaeal chromatin protein, with Sir2 and its regulation by acetylation. *Science 296*, 148–151.
3. Forterre, P., Confalonieri, F., and Knapp, S. (1999) Identification of the gene encoding archeal-specific DNA-binding proteins of the Sac10b family. *Mol. Microbiol. 32*, 669–670.
4. Xue, H., Guo, R., Wen, Y., Liu, D., and Huang, L. (2000) An abundant DNA binding protein from the hyperthermophilic archaeon Sulfolobus shibatae affects DNA supercoiling in a temperature-dependent fashion. *J. Bacteriol. 182*, 3929–3933.
5. Zhao, K., Chai, X., and Marmorstein, R. (2003) Structure of a Sir2 substrate, Alba, reveals a mechanism for deacetylation-induced enhancement of DNA binding. *J. Biol. Chem. 278*, 26071–26077.
6. Chou, C. C., Lin, T. W., Chen, C. Y., and Wang, A. H. (2003) Crystal structure of the hyperthermophilic archaeal DNA-binding protein Sso10b2 at a resolution of 1.85 Angstroms. *J. Bacteriol. 185*, 4066–4073.
7. Wardleworth, B. N., Russell, R. J., Bell, S. D., Taylor, G. L., and White, M. F. (2002) Structure of Alba: an archaeal chromatin protein modulated by acetylation. *Embo J. 21*, 4654–4662.
8. Xu, S., Qin, S., and Pan, X. M. (2004) Thermal and conformational stability of Ssh10b protein from archaeon Sulfolobus shibattae. *Biochem. J. 382*, 433–440.
9. Tong, Y., Cui, Q., Feng, Y., Huang, L., and Wang, J. (2002) 1H, 15N, and 13C resonance assignments and secondary structure of the Ssh10b from hyperthermophilic archaeon Sulfolobus shibatae. *J. Biomol. NMR 22*, 385–386.
10. Cui, Q., Tong, Y., Xue, H., Huang, L., Feng, Y., and Wang, J. (2003) Two conformations of archaeal Ssh10b. The origin of its temperature-dependent interaction with DNA. *J. Biol. Chem. 278*, 51015–51022.
11. Maity, H., Maity, M., and Englander, S. W. (2004) How cytochrome c folds, and why: submolecular foldon units and their stepwise sequential stabilization. *J. Mol. Biol. 343*, 223–233.
12. Cavanagh, J. (1996) *Protein NMR Spectroscopy: Principles and Practice*, Academic Press, San Diego.
13. Vuister, G. W., and Bax, A. (1993) Quantitative J correlation: a new approach for measuring homonuclear three-bond J(HNH.alpha.) coupling constants in 15N-enriched proteins. *J. Am. Chem. Soc. 115*, 7772–7777.
14. Farrow, N. A., Muhandiram, R., Singer, A. U., Pascal, S. M., Kay, C. M., Gish, G., Shoelson, S. E., Pawson, T., Forman-Kay, J. D., and Kay, L. E. (1994) Backbone dynamics of a free and phosphopeptide-complexed Src homology 2 domain studied by 15N NMR relaxation. *Biochemistry 33*, 5984–6003.
15. Markley, J. L., Bax, A., Arata, Y., Hilbers, C. W., Kaptein, R., Sykes, B. D., Wright, P. E., and Wuthrich, K. (1998) Recommendations for the presentation of NMR structures of proteins and nucleic acids. IUPAC-IUBMB-IUPAB Inter-Union Task Group on the Standardization of Data Bases of Protein and Nucleic Acid Structures Determined by NMR Spectroscopy. *J. Biomol. NMR 12*, 1–23.
16. Nilges, M., and O'Donoghue, S. I. (1998) Ambiguous NOEs and automated NOE assignment. *Prog. Nucl. Magn. Reson. Spectrosc. 32*, 107–139.
17. Linge, J. P., O'Donoghue, S. I., and Nilges, M. (2001) Automated assignment of ambiguous nuclear overhauser effects with ARIA. *Methods Enzymol. 339*, 71–90.
18. Linge, J. P., Habeck, M., Rieping, W., and Nilges, M. (2003) ARIA: automated NOE assignment and NMR structure calculation. *Bioinformatics 19*, 315–316.
19. Nilges, M. (1993) A calculation strategy for the structure determination of symmetric dimers by 1H NMR. *Proteins 17*, 297–309.
20. Folmer, R. H., Hilbers, C. W., Konings, R. N., and Nilges, M. (1997) Floating stereospecific assignment revisited: application to an 18 kDa protein and comparison with J-coupling data. *J. Biomol. NMR 9*, 245–258.
21. Linge, J. P., and Nilges, M. (1999) Influence of non-bonded parameters on the quality of NMR structures: a new force field for NMR structure calculation. *J. Biomol. NMR 13*, 51–59.
22. Laskowski, R. A., Rullmannn, J. A., MacArthur, M. W., Kaptein, R., and Thornton, J. M. (1996) AQUA and PROCHECK-NMR: programs for checking the quality of protein structures solved by NMR. *J. Biomol. NMR 8*, 477–486.
23. Xie, T., Liu, D., Feng, Y., Shan, L., and Wang, J. (2007) Folding stability and cooperativity of the three forms of 1−110 residues fragment of staphylococcal nuclease. *Biophys. J. 92*, 2090–2107.
24. Dosset, P., Hus, J. C., Blackledge, M., and Marion, D. (2000) Efficient analysis of macromolecular rotational diffusion from heteronuclear relaxation data. *J. Biomol. NMR 16*, 23–28.
25. Pawley, N. H., Wang, C., Koide, S., and Nicholson, L. K. (2001) An improved method for distinguishing between anisotropic tumbling and chemical exchange in analysis of 15N relaxation parameters. *J. Biomol. NMR 20*, 149–165.
26. Bai, Y., Milne, J. S., Mayne, L., and Englander, S. W. (1993) Primary structure effects on peptide group hydrogen exchange. *Proteins 17*, 75–86.
27. Bai, Y., Sosnick, T. R., Mayne, L., and Englander, S. W. (1995) Protein folding intermediates: native-state hydrogen exchange. *Science 269*, 192–197.
28. Connelly, G. P., Bai, Y., Jeng, M. F., and Englander, S. W. (1993) Isotope effects in peptide group hydrogen exchange. *Proteins 17*, 87–92.
29. Jaravine, V. A., Rathgeb-Szabo, K., and Alexandrescu, A. T. (2000) Microscopic stability of cold shock protein A examined by NMR native state hydrogen exchange as a function of urea and trimethylamine N-oxide. *Protein Sci. 9*, 290–301.
30. Bai, Y., Milne, J. S., Mayne, L., and Englander, S. W. (1994) Protein stability parameters measured by hydrogen exchange. *Proteins 20*, 4–14.
31. Chamberlain, A. K., Handel, T. M., and Marqusee, S. (1996) Detection of rare partially folded molecules in equilibrium with the native conformation of RNaseH. *Nat. Struct. Biol. 3*, 782–787.
32. Zeeb, M., Lipps, G., Lilie, H., and Balbach, J. (2004) Folding and Association of an Extremely Stable Dimeric Protein from Sulfolobus islandicus. *J. Mol. Biol. 336*, 227–240.
33. Cai, M., Gong, Y. X., Wen, L., and Krishnamoorthi, R. (2002) Correlation of binding-loop internal dynamics with stability and function in potato I inhibitor family: relative contributions of Arg(50) and Arg(52) in Cucurbita maxima trypsin inhibitor-V as studied by site-directed mutagenesis and NMR spectroscopy. *Biochemistry 41*, 9572–9579.
34. Wu, X., Oppermann, M., Berndt, K. D., Bergman, T., Jonvall, H., Knapp, S., and Oppermann, U. (2008) Thermal unfolding of the archaeal DNA and RNA binding protein Ssh10. *Biochem. Biophy. Res. Commun.* , doi:10.1016/j.bbrc.2008.06.030, in press.
35. Gouet, P., Robert, X., and Courcelle, E. (2003) ESPript/ENDscript: Extracting and rendering sequence and 3D information from atomic structures of proteins. *Nucleic Acids Res. 31*, 3320–3323.
36. Wang, G., Guo, R., Bartlam, M., Yang, H., Xue, H., Liu, Y., Huang, L., and Rao, Z. (2003) Crystal structure of a DNA binding protein from the hyperthermophilic euryarchaeon Methanococcus jannaschii. *Protein Sci. 12*, 2815–2822.
37. Leone, M., Di Lello, P., Ohlenschlager, O., Pedone, E. M., Bartolucci, S., Rossi, M., Di Blasio, B., Pedone, C., Saviano, M., Isernia, C., and Fattorusso, R. (2004) Solution structure and backbone dynamics of the K18G/R82E Alicyclobacillus acidocaldarius thioredoxin mutant: a molecular analysis of its reduced thermal stability. *Biochemistry 43*, 6043–6058.
38. Jaenicke, R., and Bohm, G. (1998) The stability of proteins in extreme environments. *Curr. Opin. Struct. Biol. 8*, 738–748.
39. Yano, J. K., and Poulos, T. L. (2003) New understandings of thermostable and peizostable enzymes. *Current Opin. Biotechnol. 14*, 360–365.
40. Jaenicke, R. (2000) Do ultrastable proteins from hyperthermophiles have high or low conformational rigidity? *Proc. Natl. Acad. Sci. U.S.A. 97*, 2962–2964.
41. Zavodszky, P., Kardos, J., Svingor, and Petsko, G. A. (1998) Adjustment of conformational flexibility is a key event in the thermal adaptation of proteins. *Proc. Natl. Acad. Sci. U.S.A. 95*, 7406–7411.
42. Elcock, A. H. (1998) The stability of salt bridges at high temperatures: implications for hyperthermophilic proteins. *J. Mol. Biol. 284*, 489–502.

BI8007593